ACS OMEGA

http://pubs.acs.org/journal/acsodf

Article

Molecular Weight Controls Interactions between Plastic Deformation and Fracture in Cold Spray of Glassy Polymers

Jeeva Muthulingam, Anuraag Gangineri Padmanaban, Nand K. Singh, Tristan W. Bacha, Joseph F. Stanzione, III, Francis M. Haas, Ratneshwar Jha, Jae-Hwang Lee, and Behrad Koohbor*

Cite This: *ACS Omega* 2023, 8, 3956−3970

Read Online

ACCESS | Metrics & More | Article Recommendations

ABSTRACT: Polymer cold spray has gained considerable attention as a novel manufacturing process. A promising aspect of this technology involves the ability to deposit uniform polymer coatings without the requirements of solvent and/or high-temperature conditions. The present study investigates the interplay between shear instability, often considered to be the primary mechanism for bond formation, and fracture, as a secondary energy dissipation mechanism, collectively governing the deposition of glassy thermoplastics on similar and dissimilar substrates. A hybrid experimental-computational approach is utilized to explore the simultaneous effects of several interconnected phenomena, namely the particle−substrate relative deformability, molecular weights, and the resultant yielding versus fracture of polystyrene particles, examined herein as a model material system. The computational investigations are based on constitutive plasticity and damage equations determined and calibrated based on a statistical data mining approach applied to a wide collection of previously reported stress−strain and failure data. Results obtained herein demonstrate that the underlying adhesion mechanisms depend strongly on the molecular weight of the sprayed particles. It is also shown that although the plastic deformation and shear instability are still the primary bond formation mechanisms, the molecular-weight-dependent fracture of the sprayed glassy polymers is also a considerable phenomenon capable of significantly affecting the deposition process, especially in cases involving the cold spray of soft thermoplastics on hard substrates. The strong interplay between molecular-weight-dependent plastic yielding and fracture in the examined system emphasizes the importance of molecular weight as a critical variable in the cold spray of glassy polymers, also highlighting the possibility of process optimization by proper feedstock selection.

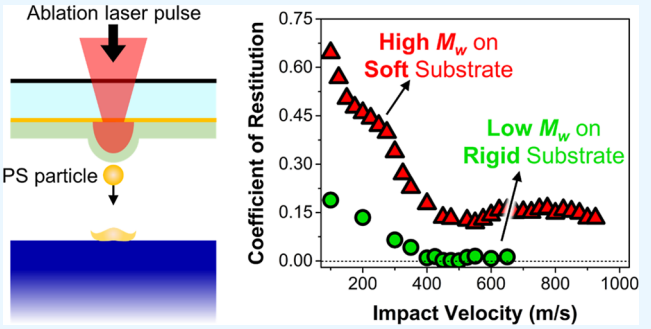

1. INTRODUCTION

Cold spray is a solid-state additive manufacturing/coating process wherein microparticles are accelerated inside a convergent-divergent nozzle and sprayed toward a substrate with high kinetic energy.[1] Upon impact, particles adhere to the substrate to create a low porosity coating of relatively uniform thickness. Depending on the particle−substrate material pair, the nature of the bond formation can be either metallurgical, chemical, or mechanical. Irrespective of the nature of the bonds formed, the occurrence of severe plastic deformation at the particle/substrate interface plays a major role in the adhesion process.[2] The main advantage of cold spray over other additive manufacturing processes is that the melting of particle in flight and/or substrate can be suppressed, thereby mitigating material degradation and oxidation while lowering the overall thermal residual stresses and their detrimental effects on the integrity of the product.[3−6]

Manufacturing of polymers and polymer-based composites has been facilitated by concurrent advances in cold spray technology and growth in the number of applications of polymers in various industries.[5−11] When used as cold spray feedstock, polymer particles behave quite differently than metals. The differences between the impact response of polymeric and metallic feedstock mainly originate from the significant differences in their thermo-mechanical properties, the nature of the bonds formed (e.g., metallurgical and metallic bonds in metal cold spray, which do not necessarily apply to polymer cold spray), as well as the material's location on the crystalline-amorphous spectrum. Regardless, the occurrence of extremely high strains and strain rates in both the impacting particles and the substrate is the main driving force for a

Received: October 13, 2022
Accepted: December 21, 2022
Published: January 20, 2023

successful deposition of cold-sprayed powders.[10−14] The high local strain fields developed at the particle−substrate interface vicinity lead to adiabatic heating and substantial local thermal softening, effectively improving the mixing between the two components.[9−11] However, when both the particle and the substrate are polymers, other mechanisms can arise subsequent to the local heating: mechanical mixing, interlocking, and entanglement between the polymer in the impacting particle and the polymer constituent in the substrate. In such cases, the rheological behavior of the constituent polymer species can also play a major role in the establishment and strength of the bond.[12−16]

Considering the growing interest in polymer cold spray, studies have been dedicated to understanding the underpinnings of this process. For example, Bush et al.[4] demonstrated through an experimental study the successful deposition of high-density polyethylene particles onto various polymeric and non-polymeric substrates. They found that the adhesion between HDPE particles and various substrates requires impact velocities exceeding 100 m/s. In addition, their study highlighted the effects of particle diameter, velocity, and initial temperature on deposition efficiency, showing that deposition efficiency increases with an increase in particle velocity and initial temperature. Khalkhali et al.[5] conducted single-particle impact experiments on polyamide 12 and polystyrene (PS) particles on PA and low-density polyethylene (LPDE) substrates. This work reported deposition velocity windows in the range of 120−140 and 170−180 m/s for PS on LPDE and polyamide 12 on LPDE, respectively. Based on their findings, polymers with a lower glass transition temperature (T_g) were reported to possess the ability to deposit at lower impact velocities and with higher deposition efficiencies. As such, the significant role of temperature was further highlighted by preheating polymer particles above their glass transition temperature, confirming particle preheating as a practical solution to achieve higher deposition efficiencies and a low-porosity deposit. Singh et al.[9] reported the effect of relative deformability of particles and substrates on deposition mechanisms of polyetheretherketone (PEEK), acrylonitrile−butadiene−styrene, and copper particles on PEEK substrates. Their numerical findings indicated that the deposition is governed by the plastic deformation of the particle in soft particle/hard substrate cases. On the other hand, the extensive plastic deformation of the substrate is critical in activating a mechanical interlocking mechanism that facilitates a successful deposition in hard particle/soft substrate conditions, for example, copper on PEEK. Yang et al.[8] demonstrated the successful deposition of polymeric particles with a core−shell structure composed of epoxy resin surrounded by poly (methyl methacrylate) on an aluminum substrate using a laser-induced single-particle impact experiment. They found that the critical velocity for deposition can be decreased drastically by lowering the glass transition temperature of the polymer core. Bae et al.[19] conducted numerical and experimental studies on metallic particles to demonstrate that the critical velocity decreases when the substrate is more rigid than the particle. A similar study was conducted by Shah et al.[10] for both polymeric and non-polymeric substrates. The results indicated that a softer particle experiences larger plastic deformation upon impact, effectively increasing the contact area and temperature at the interface and eventually leading to stronger bonding. Ravi et al.[20] deposited ultra-high molecular weight polyethylene onto an aluminum substrate using cold spray. Their results demonstrated that a successful deposition was only possible when small quantities of alumina nanoparticles were incorporated into the polymeric powders, improving inter-particle adhesion by providing additional surface functionality. A recent report by Shan et al.[21] showed that the deformation response of PS microparticles in ultra-high strain rate impact is strongly dependent upon molecular weight. It was concluded in this work that the interactions between molecular entanglements, temperature, shear strain, and the strain rate govern the degree of plastic deformation and the particle's failure behavior, thereby affecting the energy dissipation mechanisms upon impact.

The survey of the literature on polymer cold spray indicates a growing interest in the study of dissimilar coating, especially those wherein softer particles are to be deposited on hard substrates. Despite the significant scientific understandings presented thus far, there still exist major gaps in the understanding of the behavior of cold-sprayed glassy polymers, mainly due to complexities arising from their brittle nature. In particular, there is still insufficient understanding of the interplay between plastic deformation (as the major mechanism for bonding in polymer cold spray) and the possible roles of fracture and state transformation as two secondary mechanisms attributing to the dissipation of kinetic energy of the particles.[21,22] The primary focus of the present work is to investigate the interplay between plastic deformation and fracture as the two primary mechanisms that govern the adhesion behavior of cold-sprayed glassy polymers. The study is designed such that the concurrent effects of the two aforementioned mechanisms, that is, plastic deformation versus failure, are investigated systematically via experimentally validated computer simulations. Although only considered an essential step in the modeling process, input material parameters for simulations are extracted using a statistical data mining approach applied to a wide collection of experimental data reported previously in the literature. These experimentally calibrated constitutive models provide a reasonable first-order representation of the mechanical behavior of the examined material at ultra-high strain rate conditions. Impact conditions are designed to enable the simultaneous study of several influencing factors, namely, the particle-to-substrate relative deformability and the PS particles' molecular weight. Results presented in the following demonstrate the major effect of molecular weight as it affects the plastic yielding versus fracture of glassy PS particles.

2. MODELING APPROACH

2.1. Finite Element Model. Thermo-mechanical behavior of PS microparticles impacting on PS and silicon (Si) substrates was modeled using a 3D finite element (FE) model created in ANSYS Autodyn/explicit dynamics in the Lagrangian framework. Figure 1 shows the schematic of the FE model geometry wherein the particle is modeled as a sphere with a diameter of d = 40 μm and the substrate as a cube with 10 × 10 × 10d dimensions. Based on previous studies, the satisfactory mesh resolution for both particle and substrate was taken to be 1/50th of the particle diameter.[15,17,23] The particles and the substrate were meshed with multizone hexahedral and 8-node brick elements, respectively. The contact condition at the particle−substrate interfaces was modeled using a constant coefficient of friction with a numerical value of 0.2.[24,25] Although not discussed here, the final simulation results were found to be only marginally

https://doi.org/10.1021/acsomega.2c06617
ACS Omega 2023, 8, 3956−3970

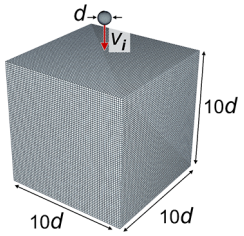

Figure 1. Geometry of the 3D FE model. Initial (impact) velocity and particle diameter are denoted by v_i and d, respectively.

sensitive to the friction coefficient value used. Except for the top (impacted) side, all other surfaces of the substrate were fully constrained. An initial downward velocity, v_i, was assigned to the entire particle volume to represent the initial (impact velocity) conditions. The velocity of the particle's center of mass was monitored to evaluate the rebound velocity, v_r, after the impact. The coefficient of restitution (CoR) was determined as the ratio of rebound to impact velocity (i.e., CoR = v_r/v_i). The CoR versus v_i curves were used as a metric to validate the modeling predictions with laser-induced projectile impact testing (LIPIT) results discussed in the forthcoming sections.

All FE simulations were performed in a system equipped with an Intel i7—12700H (2300 MHz, 14 cores) processor and a 64 GB DDR5 4800 MHz RAM. The average runtime for each case was *ca.* 10 h. The current study consists of 126 individual runs for different impact velocities and molecular weights. Therefore, the total computational cost of the current study was approximately 1260 h.

2.2. Constitutive Model. The elastic responses of the particle (PS) and the substrate (PS and Si) were assumed to be linear, isotropic, and independent of PS molecular weight.[17] The Johnson–Cook (JC) plasticity and damage models were used to describe the deformation and failure responses of the PS particles upon impact.[13,14] The JC plasticity model is widely used in modeling the high strain rate impact of materials, with increasing applications in polymer cold spray.[18−20,22] This model accounts for strain and strain rate hardening and thermal softening of the material. In the JC plasticity model, the flow stress, σ_p, is described as a function of equivalent plastic strain, ε_p, equivalent plastic strain rate, $\dot{\varepsilon}_p$, and temperature, T, as

$$\sigma_p = [A + B\,(\varepsilon_p)^n]\left[1 + C\,\ln\left(\frac{\dot{\varepsilon}_p}{\dot{\varepsilon}_{p0}}\right)\right]\left[1 - \left(\frac{T - T_r}{T_m - T_r}\right)^m\right] \quad (1)$$

where, $\dot{\varepsilon}_{p0}$ is the reference equivalent plastic strain rate; T_r and T_m are melting and reference temperatures, respectively; and coefficients A, B, n, C, and m denote the material-dependent parameters yield strength, hardening coefficient, strain hardening exponent, strain rate coefficient, and thermal softening exponent, respectively. The dependence of some of these parameters on the PS molecular weight was included in the model predictions by calibrating their relative numerical values based on previously documented data, elaborated in the next section.

The progressive damage developed in the PS particles and substrates due to high-velocity impact was investigated using the JC damage model. Specifically, the excessive deformation of an element beyond a predefined failure strain, ε_f, was used as the primary metric for failure in this work.[23,24] The PS failure strain was modeled using the following phenomenological expression

$$\varepsilon_f = [D_1 + D_2 e^{D_3\sigma^*}]\left[1 + D_4\,\ln\left(\frac{\dot{\varepsilon}_p}{\dot{\varepsilon}_{p0}}\right)\right]\left[1 + D_5\left(\frac{T - T_r}{T_m - T_r}\right)\right] \quad (2)$$

wherein, σ^* is the dimensionless stress ratio (also referred to as stress triaxiality), defined as the ratio between the hydrostatic and von Mises stresses. Given the dominant stress state, the stress ratio can take values ranging from negative to positive magnitudes. Model coefficients D_1 to D_5 are material-dependent parameters, assumed to be molecular-weight-dependent with values calibrated from literature data.

Adiabatic temperature increase due to plastic deformation, ΔT, was included in the modeling approach by using the Taylor–Quinney equation

$$\Delta T = \frac{\beta}{\rho c}\int_0^{\varepsilon_p} \sigma_p(\varepsilon_p,\ \dot{\varepsilon}_p,\ T)\mathrm{d}\varepsilon_p \quad (3)$$

where ρ and c are the mass density and heat capacity of PS, respectively. For simplicity, these two parameters were assumed to be independent of molecular weight. β in eq 3 represents the Taylor–Quinney coefficient, taken to be 0.9 in the present study.[9] Numerical values for the JC model parameters as well as all other mechanical and physical properties used in FE analyses are listed in Table 1.

Table 1. Mechanical and Physical Parameters Used as Input to the FE Analyses in This Work

		PS		
material property (units)	symbol	M_n = 100 kDa	M_n = 40 kDa	Si
elastic modulus (GPa)	E	3.11		130
density (kg/m^3)	ρ	1050		2329
Poisson's ratio	υ	0.35		0.28
specific heat (J/kg °C)	c	1260		628
melting temperature (°C)	T_m	270		
yield strength (MPa)	A	116.6	111.2	
hardening coefficient (MPa)	B	68.9	65.7	
strain hardening coefficient	N	1		
strain rate constant	C	0.0267		
softening coefficient	M	0.675		
JC damage model parameters	D_1	−1.6512	−0.04458	
	D_2	2.4587	0.06638	
	D_3	−1		
	D_4	−0.0105		
	D_5	0.327		

2.3. JC Model Parameter Calibration. JC models that describe the plasticity and damage behavior of PS, especially at ultra-high strain rates (e.g., >10^7 s^{-1}), are not available in the literature. Due to the unavailability of such experimentally validated models, the required parameters were determined based on a statistical data mining approach applied to a wide collection of PS stress–strain and failure data extracted from multiple sources.[26−33]

First, to calibrate the strain rate hardening term in eq 1, yield stress versus strain rate data extracted from various sources

https://doi.org/10.1021/acsomega.2c06617
ACS Omega 2023, 8, 3956−3970

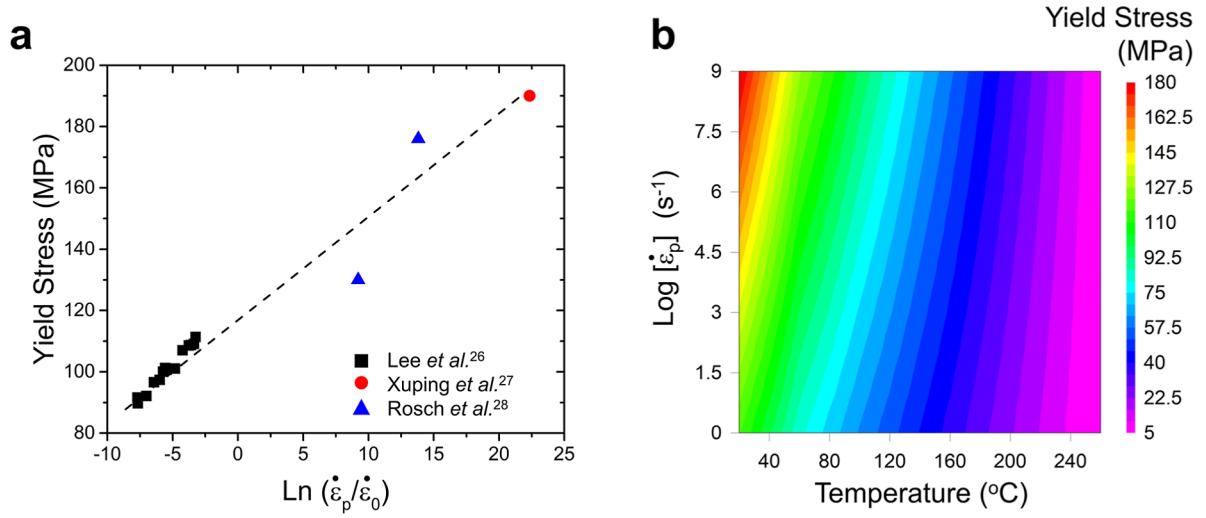

Figure 2. (a) Identification of strain rate parameter from numerical data reported in previous studies.[26−28] (b) Visualization of the 100 kDa PS yield stress as a function of temperature and the strain rate, used as input to the FE analyses.

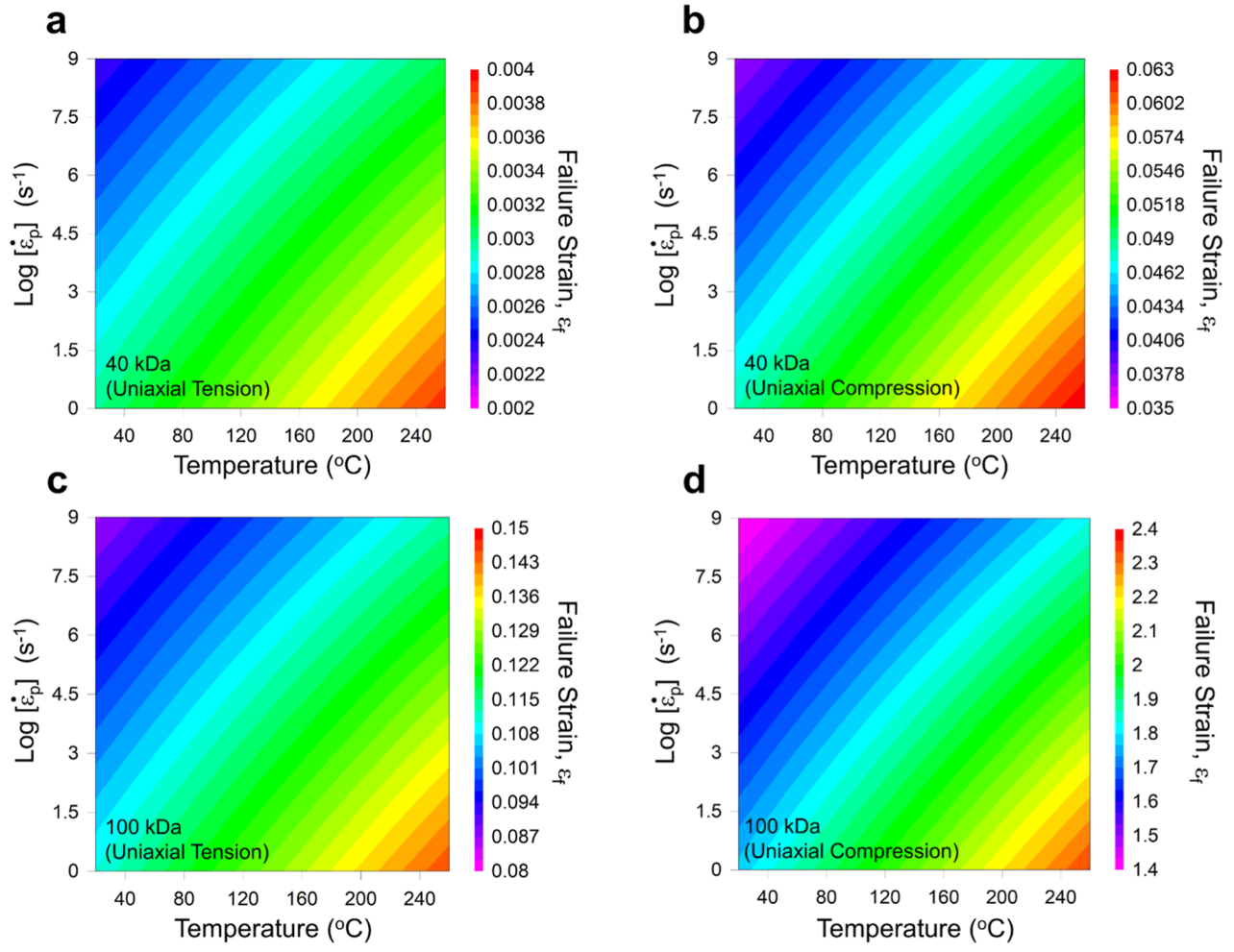

Figure 3. Variation of failure strain with respect to the strain rate and temperature for (a) M_n = 40 kDa, uniaxial tension (σ^* = 0.33), (b) M_n = 40 kDa, uniaxial compression (σ^* = −0.33), (c) M_n = 100 kDa, uniaxial tension (σ^* = 0.33), and (d) M_n = 100 kDa, uniaxial compression (σ^* = −0.33).

were plotted. The slope of the best linear fit to the yield stress−strain rate data (see Figure 2a) was identified as the strain rate coefficient, C. Similarly, the thermal softening exponent, m, was identified by linear regression of a large number of scattered yield stress-temperature data points extracted from previous reports.[31] Finally, the strain hardening parameters, B and n, were identified by finding the slope of the best linear fit to the $\log(\sigma_p - A) - log(\varepsilon_p)$ curves at the

https://doi.org/10.1021/acsomega.2c06617
ACS Omega 2023, 8, 3956−3970

reference strain rate and temperature conditions of $\dot{\varepsilon}_{p0} = 1\ s^{-1}$ and $T_r = 20\ °C$, respectively. The slope of this linear fit is equal to $\log(n)$, and the y-intercept denotes $\log(B)$. The method described above was applied to material data reported for PS with $M_n = 100$ kDa, first. The same approach was then used to identify the same set of parameters for PS with $M_n = 40$ kDa. To minimize the number of independent variables, the molecular weight was assumed to affect the yield stress, A, and the hardening coefficient, B, only, whereas all other JC plasticity coefficients were assumed to be independent of PS molecular weight. Visual representation of the PS yield stress as a function of the strain rate and temperature for $M_n = 100$ kDa PS is depicted in Figure 2b.

A similar approach was followed to calibrate the JC damage model parameters (D_1 to D_5 in Eq. 2). Due to the scarcity of failure strain data for various strain rates, temperatures, and stress states, the coefficient D_3 was assumed to be constant with a numerical value set to -1 for simplicity. A negative value for D_3 ensures a larger failure strain for compression-dominant stress states. Parameters D_1 and D_2 were calibrated by fitting a collection of failure strain versus stress ratio data obtained from various sources, reporting the failure strains for PS under uniaxial compression ($\sigma^* = -0.33$) and uniaxial tension ($\sigma^* = 0.33$) tests at reference strain rate and temperature conditions.[32,33] After calibrating the numerical values for D_1 and D_2, a similar approach was applied to calibrate the two remaining constants, D_4 and D_5, for elevated strain rate and temperature conditions. While the latter two coefficients were assumed to be independent of PS molecular weight, the first two coefficients, that is, D_1 and D_2 were calibrated for molecular weights of $M_n = 40$ and 100 kDa. Table 1 shows all JC model parameters used for the modeling in this work. Figure 3 shows the variation of failure strain with respect to the strain rate and temperature for the two molecular weights considered herein and two stress states, uniaxial compression and uniaxial tension.

It must be emphasized here that the statistics-based parameter calibration approach described above has no physical interpretation and is only proposed as a practical means to facilitate FE analyses. In that sense, the molecular-weight-dependent JC models in the present study should only be considered as a reasonable first-order representation of previously observed material behavior at high strain rate conditions. Furthermore, the authors are uncertain whether the reasonable model predictions (as validated by experiments, detailed in the forthcoming sections) can be extended to conditions beyond those described in the present article. In particular, because the model parameter calibration has been conducted based on two molecular weights, the validation of JC model parameters for other molecular weights may not be guaranteed. Nevertheless, as discussed in the following, the agreement between model predictions and single particle impact tests leads us to assume that the model-predicted mechanical behavior of PS particle impact in this work is relevant and reliable, at least for comparative purposes.

3. EXPERIMENTS

3.1. Material Preparation. PS particles with monodisperse size and molecular weight distributions were prepared using the co-flow microfluidic device described by Bacha et al.[34] Both 40 kDa (PSS GmbH, Mainz, Germany) and 100 kDa (Scientific Polymer Products Inc., Ontario, NY) PSs were dissolved in ethyl acetate and diluted to 5% w/v before being dispersed into a solution of water and 2% w/v polyvinyl alcohol by the microfluidic device. The polydispersity index was 1.04 for both PSs, as reported by the manufacturers. After production, particles were dried according to the procedures detailed in Padmanaban et al.,[22] where the production of the heat-cast 100 kDa PS substrates is also described in the corresponding Supporting Information. Scanning electron microscopy (SEM) images of the dry particles are given in Figure 4. Note that small divots on the surfaces of the particles

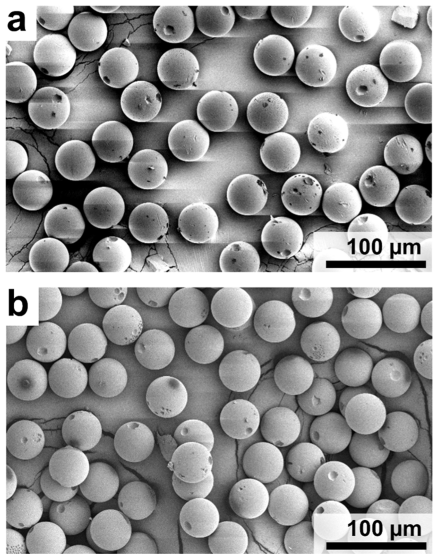

Figure 4. SEM images of (a) 40 and (b) 100 kDa PS particles. Particle sizes of 40.56 ± 1.24 and 39.69 ± 1.05 μm were determined for the 40 and 100 kDa molecular weight PS particles, respectively.

are a result of the multiphase solvent removal process. Bubbles of a water-rich phase migrate outside the concentrated PS/ethyl acetate phase, leaving an imprint as the particles harden.

3.2. Laser-Induced Projectile Impact Testing. Figure 5a shows the experimental scheme of the laser-induced projectile impact testing (LIPIT)[35,36] used to carry out single-particle impact experiments of monodispersed PS microparticles onto a flat PS or Si target. The PS microparticles were spread out evenly on a clean microscope slide using a dry brush. The microparticles were subsequently transferred onto a launch pad: a microscope cover slip (~220 μm) coated with gold (~60 nm), and cross-linked polydimethylsiloxane (PDMS; ~90 μm) elastomer. The relatively tacky PDMS layer of the launch pad picked up the PS microparticles when making contact with them on the microscope slide. A 1064 nm focused laser pulse was aligned to one of the microparticles and locally ablated the gold layer on the launching pad, resulting in the rapid expansion of the PDMS film. This rapid expansion of the PDMS film accelerated the aimed PS microparticle on top of this film at a desired velocity toward the target substrate. Ultrafast stroboscopic imaging (with illumination duration < 1 ps) was used to capture the trajectory of the microparticle showing the impacting and rebounding motions. The post-image processing yielded the travel distance of the microparticle based on the time interval between two adjacent illuminations. Thus, the impact velocity (v_i) and rebound velocity (v_r) can be accurately determined. Using LIPIT, PS microparticles were accelerated to a velocity ranging from 50 to 1000 m/s toward a

https://doi.org/10.1021/acsomega.2c06617
ACS Omega 2023, 8, 3956−3970

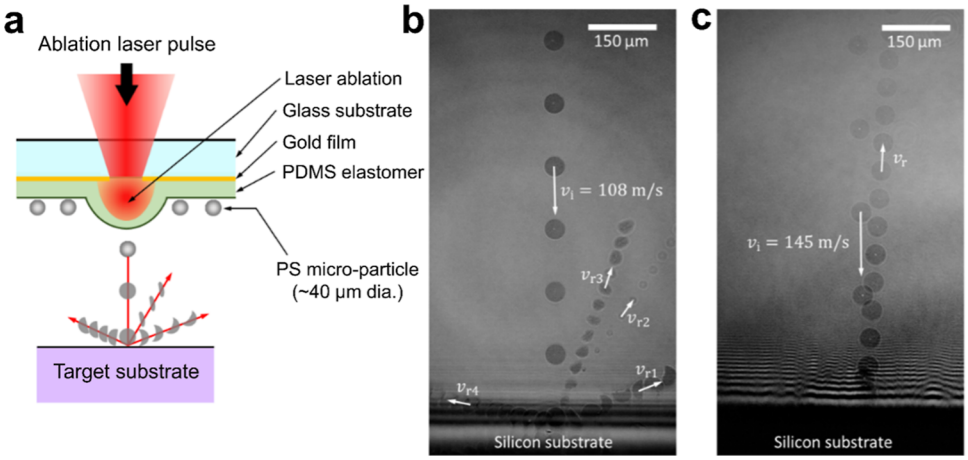

Figure 5. (a) Schematic diagram of the LIPIT experiment depicting particle fracturing upon impact. (b) Examples of LIPIT micrographs showing the impact of (b) 40 and (c) 100 kDa PS particles on Si substrates.

PS or Si target substrate. Figure 5b shows a LIPIT optical micrograph of 40 kDa PS microparticle impacting a Si substrate. Due to the low molecular weight, the microparticle exhibited very severe fracture upon impact compared to the 100 kDa microparticles as shown in Figure 5c. In the case of a fractured collision, the mean value of individual rebound velocities of the shattered fragments was used to define the representative rebound velocity of the fractured collision.

4. RESULTS AND DISCUSSION

4.1. Experimental Validation of Model Predictions. Two metrics were utilized to validate the FE model predictions in this work. First, the variation of the CoR with respect to impact velocity, obtained from LIPIT and FE analyses, were compared. Figure 6 shows the CoR-v_i curves obtained from the

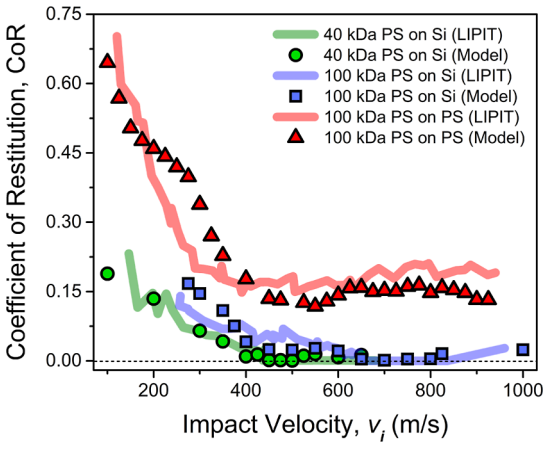

Figure 6. Variation of CoR values with impact velocity for PS particles with 40 and 100 kDa molecular weights and two substrates (PS and Si). The continuous lines represent experimental (LIPIT) measurements. Scattered symbols represent results from FE analyses.

two independent approaches. The close agreement between the magnitudes and the trends in the two data sets suggests the reliability of the modeling approach. More importantly, the zero CoR windows, representing the deposition window (discussed in detail in the forthcoming sections), are replicated by modeling predictions. Interestingly, these deposition windows are found to occur only in the case of Si substrates and at different impact velocity ranges depending on the PS molecular weight. The latter will be discussed in more detail in later sections.

In addition to CoR characteristics, the post-impact particle morphologies obtained from LIPIT and FE analyses were also compared and used as another metric to validate the model-predicted results in the present study. Following the approach discussed in Chen et al.,[37] the post-impact morphology of a plastically deformed particle can be represented by the aspect ratio of its orthogonal diameters, $R = D_1/D_2$, where D_1 and D_2 denote the major and minor diagonals of the deformed particle, respectively. Note that the 2D nature of the images acquired during LIPIT makes it impractical to consider the 3D geometry of the post-impact particles. Nevertheless, the post-impact aspect ratio parameter was determined for various LIPIT experiments by tracking the exterior outline of the deformed particle, an example of which has been shown in Figure 7a. The same process was applied to determine the outline of the post-impact particle obtained from FE analyses. A one-to-one comparison between the results obtained independently from LIPIT and FE analyses for the 100 kDa PS-on-PS impact is shown in Figure 7e, confirming a good agreement between experiments and simulations in this work. Note that the post-impact shape comparisons were only possible for the PS-on-PS impact, as the PS particles impacting Si substrates were heavily damaged and adhered to the substrate at specific velocities, making it impossible to characterize the particle outline. Nevertheless, the good match between experimental and simulation results, quantified by two independent metrics, supports the validity of the modeling framework.

4.2. M_n-Dependent CoR. CoR is considered the primary metric for the adhesion versus rebound of the PS particles in this work. Consistent with the LIPIT results, model predictions also suggest that the adhesion of PS particles on the PS substrate is not possible. The role of initial particle temperature to increase the possibility of PS-on-PS adhesion was also investigated by assigning an initial temperature of 90 °C to the PS particles. Figure 8a shows the CoR trends obtained for PS particles on PS substrates for two molecular weights and two initial particle temperatures. Note that the 90 °C initial particle temperature was selected due to its proximity to the glass transition temperature of the two molecular weights studied here, that is, T_g = 97.3 and 96.4 °C for M_n = 40 and 100 kDa,

https://doi.org/10.1021/acsomega.2c06617
ACS Omega 2023, 8, 3956−3970

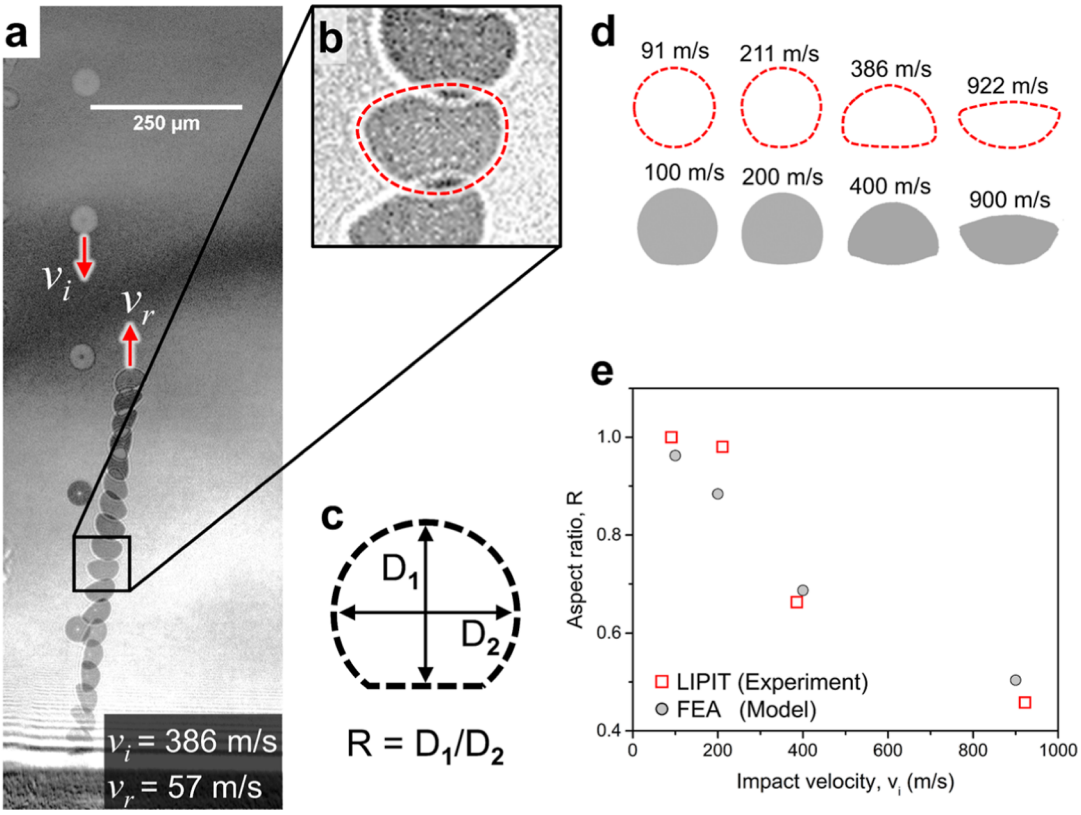

Figure 7. (a) Example of a stroboscopic micrograph of a PS particle impacting the PS substrate at an impact velocity of 386 m/s. (b) Close-up view of the rebounded, deformed particle with its outline marked by a dashed red curve. (c) Schematic view and the definition of the post-impact aspect ratio. (d) Experimental (top row) and simulated (bottom row) morphology of the post-impact PS particles at different impact velocities. (e) Variation of the post-impact aspect ratio with impact velocity for PS (100 kDa) particles impacting PS substrates.

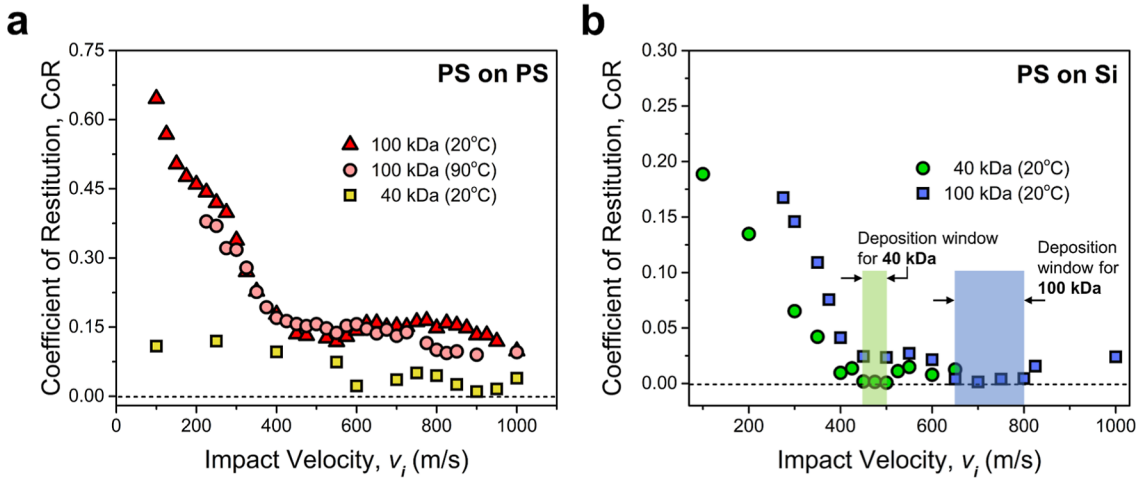

Figure 8. CoR value predicted by the FE model at different impact velocities for PS particles impacting (a) PS and (b) Si substrates. Results presented for PS particles with 40 and 100 kDa molecular weights and two initial particle temperatures of 20 and 90 °C.

respectively.[22] As shown in Figure 8a, higher particle temperatures tend to lower the CoR trends for Ps-on-Ps impact. However, there is no indication of adhesion (CoR = 0), regardless of temperature and/or molecular weight. Model-predicted CoR trends can be interpreted by considering the initial kinetic energy of the particle upon impact. Irrespective of particle temperature and molecular weight, the impact response of the particle at lower velocities is dominated by the elastic co-deformation of the particle and the substrate. At low impact velocities, an elastic-dominated impact leads to the retention of all or a significant portion of the initial kinetic energy, thereby causing the recoiling of the PS particle. Higher initial temperatures and/or lower molecular weights reduce the resistance of the particle to plastic (inelastic) deformation, consequently decreasing the dominant elastic recoiling effect. As such, the CoR values tend to decrease for lower molecular weights and higher temperatures, especially in the lower impact velocity ranges. Nonetheless, the CoR trends for PS-on-PS impact do not show any evidence of adhesion at any velocity range, even for lower (40 kDa) molecular weights. On the

https://doi.org/10.1021/acsomega.2c06617
ACS Omega 2023, 8, 3956−3970

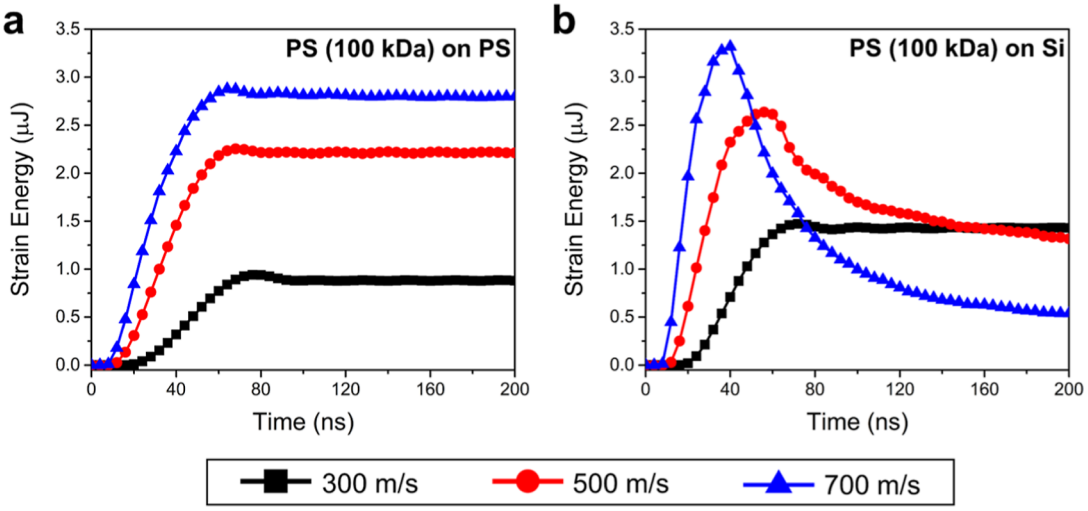

Figure 9. Temporal evolution of strain energy for 100 kDa PS particles impacting on (a) PS and (b) Si substrates at three impact velocities of 300, 500, and 700 m/s.

other hand, a similar comparison made on the PS particles impacting Si substrates suggests the existence of a deposition (adhesion) window which occurred at v_i = 450−500 m/s and v_i = 650−800 m/s for M_n = 40 and 100 kDa, respectively, as shown in Figure 8b. In the PS-on-Si case also, a decrease in the molecular weight contributes to the overall lowering of CoR values as well as the velocity range of the deposition window. The possibility of depositing low molecular weight PS particles on the PS substrate was previously reported in the work of Khalkhali et al.[5] for conditions wherein the substrate temperature was maintained at 100 °C, that is, above the glass transition temperature.

Considering that the Si substrate has a significantly higher stiffness than the PS counterpart, in addition to the fact that the Si substrate was modeled as a perfectly linear elastic (with no plastic yielding) solid, the results obtained herein seem contradictory to the fundamental understanding of adhesion in polymer (and metal) cold spray. That is to say, the occurrence of plastic deformation at the particle−substrate interface is the major mechanism by which the kinetic energy of the incoming particle is dissipated. Thus, the particle−substrate adhesion is more likely when severe plastic deformations occur. The possible roles and interconnections between particle/substrate temperature variations, plastic deformation, and fracture are further investigated to address the counterintuitive results obtained from the model predictions (also verified by LIPIT data[22]) in this work.

4.3. M_n-Dependent Energy Dissipation Mechanisms. Probing the energy level of a particle can be used as a metric to quantify its holistic impact behavior. As such, the temporal variation of the net strain energy for different molecular weights, substrates, and impact velocities are studied here. Before embarking on further details, it should be noted that the strain energy metric used herein is calculated by integrating the stress−strain response of an impacted particle over its entire initial volume, multiplied by a factor termed the current volume. The current volume refers to the load-bearing volume of the particle that remains attached to the body of the original spherical particle after impact. In other words, due to the occurrence of significant failure in certain conditions (discussed in detail later), parts of an impacted particle may be detached and disintegrated from the original volume, becoming inactive in impact energy dissipation.

Figure 9 shows the temporal evolution of strain energy for PS particles with 40 and 100 kDa molecular weights, impacting PS and Si substrates at three representative impact velocities. The general trends observed in this figure vary strongly based on impact conditions. First, as shown in Figure 9a, the energy curves obtained for 100 kDa PS particle impacting PS substrates are exemplified by an initial increase, followed by a slight decrease and then an extended plateau. The slope of the initial increase in all curves is directly correlated with the impact velocity. That is, a higher velocity impact simply subjects the particle to a higher strain rate deformation, thus increasing the rate at which strain energy is dissipated through the particle volume. The high rate increase of energy in Figure 9a is followed by a slight decrease due to the elastic strain energy recovered upon the rebound of the particle from the substrate. Finally, the energy plateaus are indicative of a "saturation phase" wherein the particle bounces back from the substrate with no further plastic deformation. The latter implies that irrespective of the velocity, the impact of 100 kDa PS particles on the PS substrate will not lead to deposition, as was also demonstrated by the CoR results in Figure 8a. Note that in the case of PS substrates, a portion of the incoming kinetic energy is also dissipated through plastic deformation of the substrate, as will be discussed later.

Substituting the PS substrate with higher stiffness, the linearly elastic Si substrate substantially alters the general shapes of the energy curves for the 100 kDa PS particle, as shown in Figure 9b. In such cases, the maximum energy levels developed in the particle are higher than those previously observed for 100 kDa PS-on-PS impact. This relative increase in the maximum energy dissipation is due to the larger plastic deformations developed in PS particles as a consequence of an impact on elastic Si substrates, noting that the linearly elastic Si substrates in this work do not contribute to energy dissipation. For the 300 m/s impact, the overall shape of the energy curve for 100 kDa PS-on-Si is similar to those in Figure 9a, indicating a low energy dissipation and an unsuccessful adhesion. However, at higher (i.e., 500 and 700 m/s) impact velocities, a significant and progressive decrease in the energy levels are observed. Particularly, the 700 m/s impact of the 100 kDa PS

https://doi.org/10.1021/acsomega.2c06617
ACS Omega 2023, 8, 3956−3970

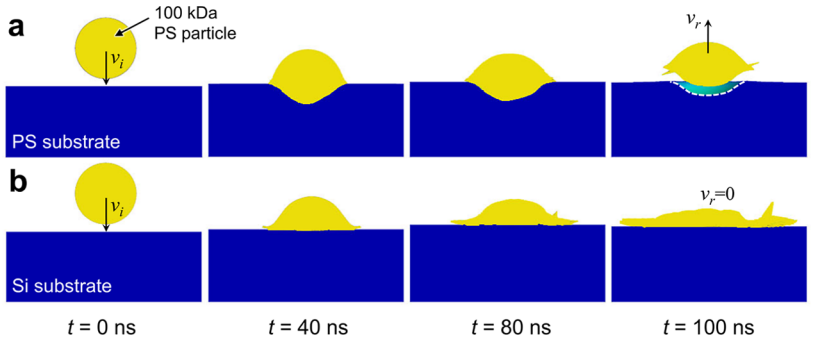

Figure 10. Time sequence snapshots showing the impact of 100 kDa PS particle (shown in yellow) on (a) PS and (b) Si substrates (shown in blue) at 700 m/s. The dashed line in (a) represents the location of the crater formed in the PS substrate upon particle rebound. Severe deformation, leading to partial failure of the particle in the PS-on-Si impact is evident from the fully splattered particle in (b).

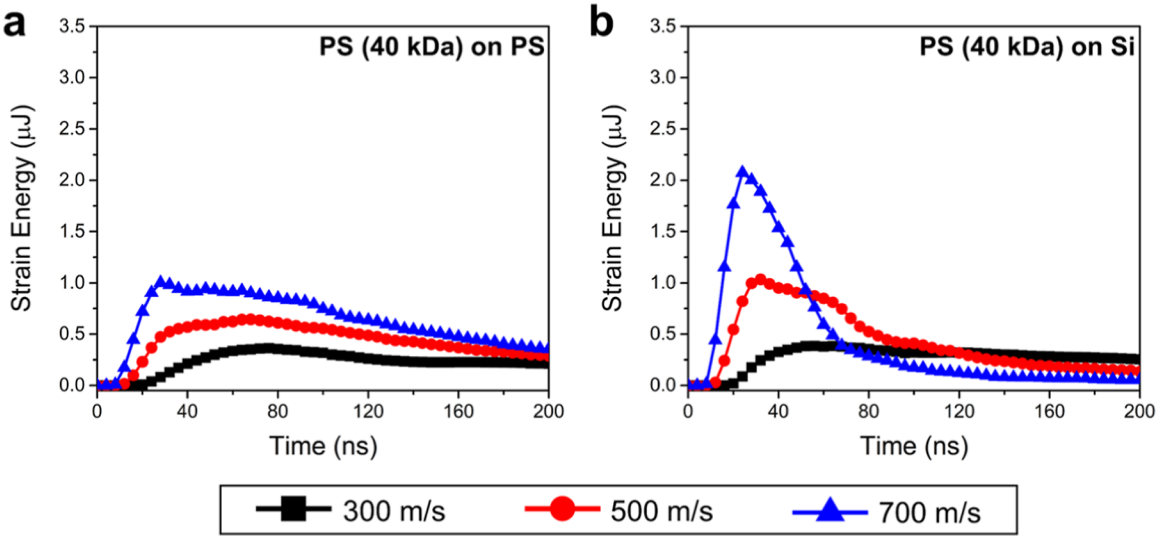

Figure 11. Temporal evolution of strain energy for 40 kDa PS particles impacting on (a) PS and (b) Si substrates at three impact velocities of 300, 500, and 700 m/s.

particle on Si shows a remarkable decrease in the strain energy after the establishment of contact. Considering that the latter condition leads to a successful deposition (CoR = 0 in Figure 8b), the energy decrease can be associated with the loss of solid load-bearing volume detached from the original particle after the impact. As such, the decrease in the effective volume of the particle reduces the net strain energy levels developed in it. A one-to-one comparison of the 100 kDa PS particle shape and morphology changes for the two substrate cases is shown in Figure 10, indicating the rebounding of the PS particle from the PS substrate with a comparatively lower degree of severe plastic deformation compared with the Si substrate. Despite the same kinetic energy in both cases, the substantially higher plastic deformation of the particle in PS-on-Si impact is exemplified by the fully splattered particle after the impact.

Energy curves shown in Figure 11 for the 40 kDa PS particles follow the overall trends described above with the following exceptions. Due to lower failure strains associated with the lower PS molecular weight (see Figure 3), the 40 kDa particles are susceptible to more significant failure upon impact on both PS and Si substrates. The absence of plateaus in energy curves in Figure 11 as well as lower overall energy levels (compared with the 100 kDa counterparts) are indicative of a more prominent effect of disintegrated volume versus plastic deformation. The proximity of particle energy levels to zero at t = 200 ns for the 40 kDa PS particles (especially in the case of the Si substrate) indicates a near complete disintegration of the deformable volume of the lower molecular weight particles after impact.

4.4. Deformation Characteristics and Temperature Evolution. The simulation results suggest that the deformation characteristics of the PS particles highly depend on their molecular weight, as well as the substrate material. Figure 12 shows the equivalent plastic deformation fields developed in the particle−substrate vicinity for different molecular weight and substrate conditions at different impact velocities. For consistency, the contour maps in Figure 12 are extracted at the time when the velocity of the particle (at its center) is zero. By comparing the shape and morphology of the particle−substrate interface vicinity, particles impacting the stiffer substrate (i.e., Si) show larger plastic deformations and a more remarkable splattering, especially at higher impact velocities. This behavior is due to the stiffer mechanical response of the Si substrate that leads to the localization of plastic deformation only in the ductile component, that is, the PS microparticle.

Another noteworthy observation in Figure 12 is the general shape of the PS particles with different molecular weights upon impact on PS substrates. In the case of lower molecular weight, the particle−substrate interface (marked by white dashed lines) seems to be broader than for the lower molecular weight

https://doi.org/10.1021/acsomega.2c06617
ACS Omega 2023, 8, 3956−3970

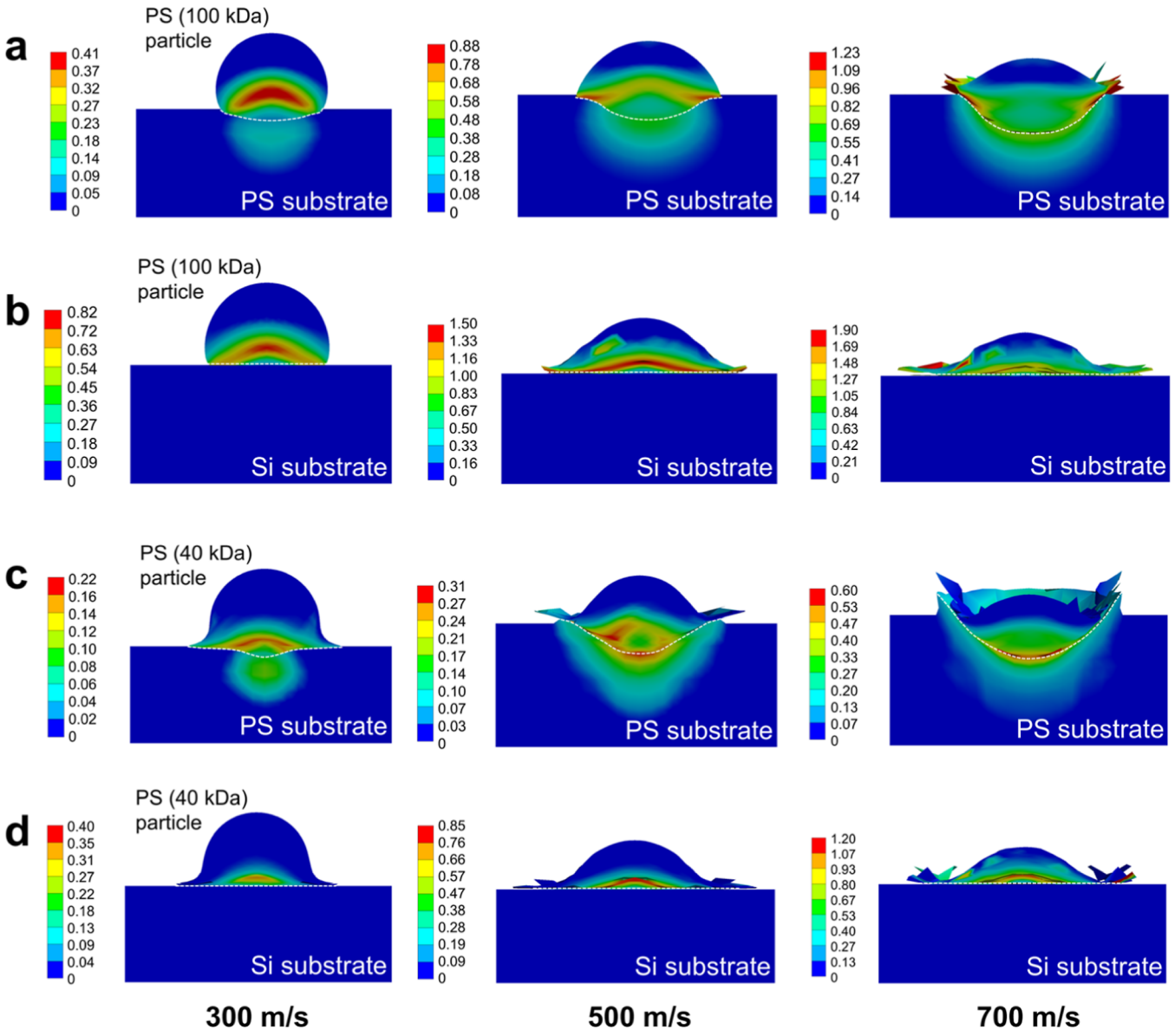

Figure 12. Contour maps showing the distribution of equivalent plastic strain in the particle−substrate vicinity for (a) 100 kDa PS particle on the PS substrate, (b) 100 kDa PS particle on the Si substrate, (c) 40 kDa PS particle on the PS substrate, and (d) 40 kDa PS particle on the Si substrate at 300 m/s (left column), 500 m/s (middle column), and 700 m/s (right column) impact velocities. Contour maps are extracted at the time instance when the velocity of the particle center is zero. Dashed lines represent the location of the particle−substrate interface.

PS-on-PS impact. In addition, comparing Figure 12a,c indicates the development of larger strain areas around the outer periphery of the impact zone in the 100 kDa PS particle. The last two observations, that is, the shape of the impact crater and the distribution/magnitude of local plastic strain, can be realized through the interplay between plastic yielding versus failure (fracture). In the case of higher molecular weight PS particles, the failure strains are significantly larger than those in the lower molecular weight counterparts. Therefore, the higher molecular weight particle tends to show a more ductile behavior by developing localized strain regions at its periphery. The same phenomenon takes place in the case of lower molecular weight PS particles, with the exception that due to lower failure strains, the 40 kDa PS particle tends to fracture at the impact periphery with limited plastic deformation. Instead, in the case of lower molecular weight particles, the lowermost region regions of the particle undergo larger plastic deformations, primarily because of the mechanical confinement (imposed by the substrate boundaries) that maintains the particle integrity.

Similar general trends can be observed when comparing the two different molecular weight PS particles impacting on the Si substrate with the following exceptions: (1) due to the absence of Si substrate ductility, the kinetic energy of an incoming particle causes excessive plastic deformation in the particle only.[38] These large plastic deformations are manifested by a noticeably more intense splattering of the particles on the Si substrate. (2) Governed by the aforementioned molecular-weight-dependent ductility versus fracture, the higher molecular weight PS particles impacting Si substrates show larger plastic strains as well as seemingly fewer failed elements (identifiable as the local geometric spikes at the outer periphery of the particles).

https://doi.org/10.1021/acsomega.2c06617
ACS Omega 2023, 8, 3956−3970

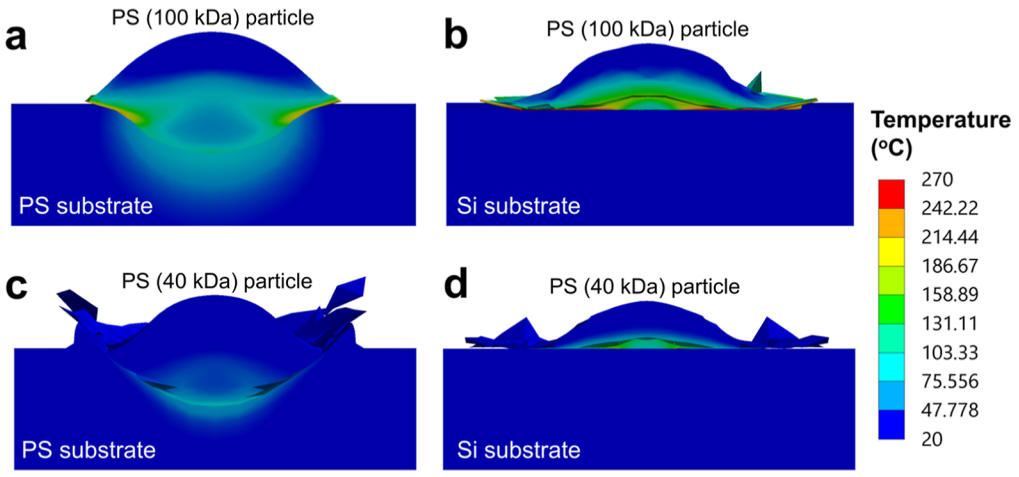

Figure 13. Contour maps showing temperature distribution in the particle−substrate vicinity for (a) 100 kDa PS particle on the PS substrate, (b) 100 kDa PS particle on the Si substrate, (c) 40 kDa PS particle on the PS substrate, and (d) 40 kDa PS particle on the Si substrate. All cases are extracted for an impact velocity of 600 m/s and at the time instance when the velocity of the particle center is zero.

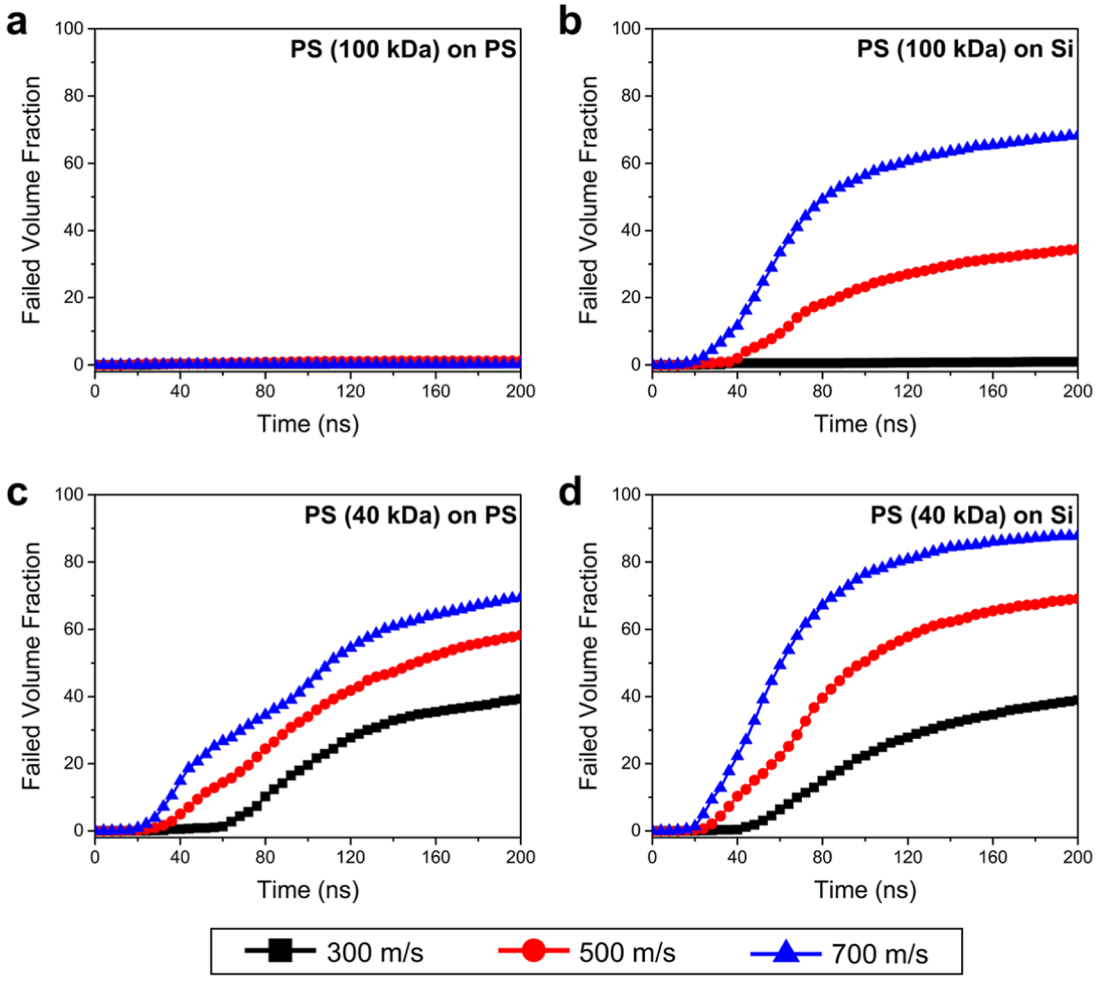

Figure 14. Temporal evolution of the particle volume fraction failed upon impact for (a) 100 kDa PS particle on the PS substrate, (b) 100 kDa PS particle on the Si substrate, (c) 40 kDa PS particle on the PS substrate, and (d) 40 kDa PS particle on the Si substrate at impact velocities of 300, 500, and 700 m/s.

From a polymer physics perspective, the increased number of entanglements and the higher interchain bonding forces in higher molecular weights contribute to the increased resistance against plastic deformation and fracture (especially considering failure under tensile stresses).[39,40] The differences between the numerical values of yield stress, hardening coefficient, and failure parameters used for the PS particles in the present simulations (see Table 1 and Figure 3) reflect these molecular-level strengthening mechanisms in a phenomenological manner. The competition between plastic deformation and

https://doi.org/10.1021/acsomega.2c06617
ACS Omega 2023, 8, 3956−3970

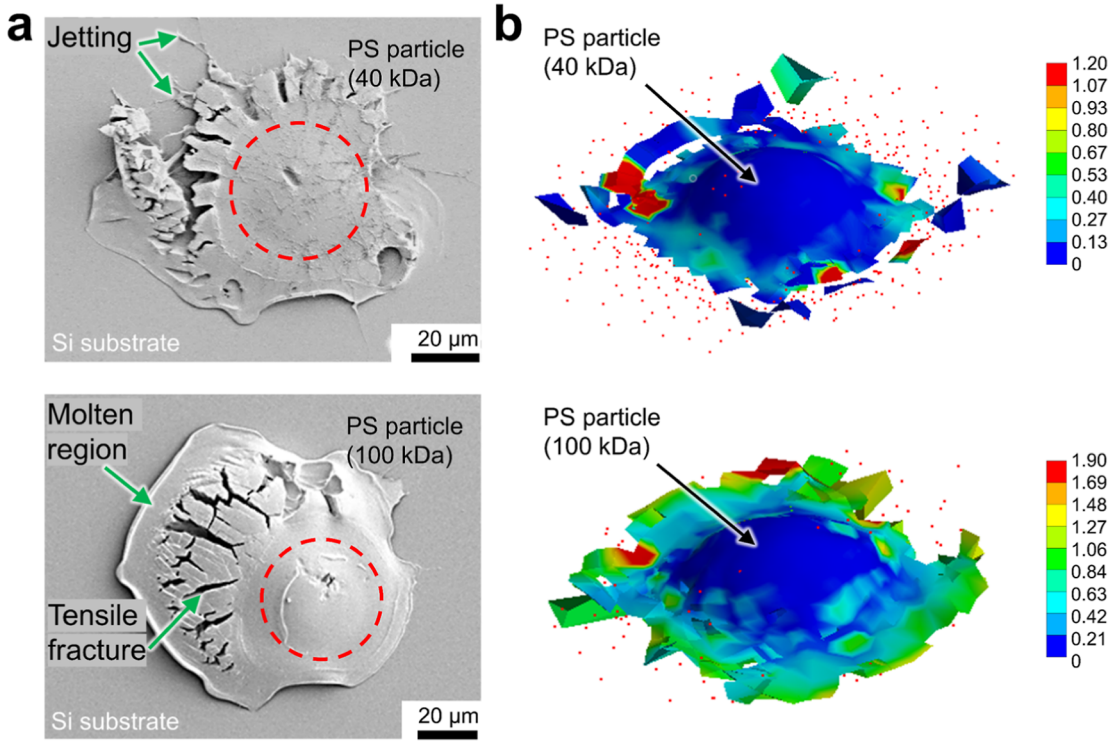

Figure 15. (a) SEM images of PS particle (top: 40 kDa, bottom: 100 kDa) after impact on the Si substrate, with the corresponding simulation results shown in (b). Contour maps in (b) show the equivalent plastic deformation fields. Dashed circles in (a) mark the initial outline of the PS particle. Scattered red dots in (b) represent the failed (eroded) elements. Impact velocity in LIPIT and FE simulations are 703 and 700 m/s, respectively.

failure in different PS molecular weights leads to vast differences in the thermal behavior of the particles as well. Figure 13 shows the temperature evolution in the particle and the substrate for different PS particle molecular weights and the two substrates. For ease of comparison, only a single impact velocity condition (v_i = 600 m/s) is examined here. In all cases, particle temperatures at the particle−substrate interface increase locally to above the PS glass transition temperature (~96−97 °C). The region of maximum particle temperature and maximum plastic deformation coincide perfectly, suggesting that the local temperature increase at the interface directly results from increased plastic deformation. This local heating effect causes the particle to deform more drastically due to local thermal softening. When combined with lower resistance against large deformations, the excessively high-temperature regions formed at the periphery of the 40 kDa PS particle lead to the formation of highly distorted elements that are detached from the particle, thus, reducing the load bearing volume of the particle. The reduced volume tends to lower the stored energy level in the particle (see Figure 11), eventually leading to significantly lower rebound velocities observed in PS-on-Si impact over a range of velocities.

Consistent with previous discussion on the plastic deformation response, temperature fields also show a strong dependence on the molecular weight and substrate material. The highest local temperatures (as high as 270 °C) have been observed in the case of 100 kDa PS on PS impact, signifying the influence of large plastic deformation as the main contributing factor in the local temperature increase in PS particles impacting stiffer substrates. These remarkably high local temperatures, mainly observed in the case of 100 kDa PS on Si (Figure 13b), have been reported to promote partial melting of the particle, favorable conditions that increase the likelihood of PS particle deposition on the Si substrate.[22]

4.5. Particle Failure Quantification and Characteristics. The influence of molecular weight on the plastic deformation and thermal behavior of the particles was discussed previously. The interplay between plastic deformation and material failure was highlighted in the previous discussion as the two competing energy dissipation mechanisms. Although the numerical quantification of the particle failure is impractical, the temporal evolution of the "failed volume fraction" of the particle can be used as a quantitative metric for comparative purposes. An impacted particle's failed volume fraction can be probed by the number of elements in the FE mesh that satisfy the failure criteria, thus becoming inactivated load-bearing components in the system.

The ratio between the number of failed elements (also referred to as "eroded elements") and the original number of elements in the particle model has been extracted for different conditions and presented in Figure 14. Consistent with previous observations, the impact of higher molecular weight PS on the PS substrate (Figure 14a) shows no indication of particle failure, confirming the dominant effect of plastic deformation for this condition, at least for impact velocities equal to or lower than 700 m/s. In contrast, the impact of 100 kDa PS particles on Si substrates is accompanied by significant failure, especially at impact velocities greater than 500 m/s. Interestingly, for the 40 kDa PS particles (see Figure 14c,d), the failed volume fractions are significant for both substrates, with those being slightly higher in the case of the Si substrate. Despite similar failure behaviors, especially comparing higher velocity impacts on PS and Si substrates, the PS-on-PS impact

https://doi.org/10.1021/acsomega.2c06617
ACS Omega 2023, 8, 3956−3970

showed no indication of deposition (as shown earlier in Figure 8).

Particle failure characteristics and their possible effect on deposition can be further investigated by directly comparing the simulations with those obtained from LIPIT experiments. Figure 15 shows the morphology of PS particles after impact on the Si substrate, comparing LIPIT and simulation results for impact velocities of *ca.* 700 m/s. The experimental observation of the 40 kDa PS impacted on Si (Figure 15a) indicates significant brittle failure and some degree of material jetting on the Si surface. The corresponding simulation also shows evidence of significant element erosion (shown by red dots in Figure 15b), suggesting the dominant effect of fracture and fragmentation as the primary mechanism for deposition. On the other hand, the deposition of 100 kDa PS on Si (Figure 15c) is exemplified by relatively lower degrees of complete disintegration while instead demonstrating evidence of tensile fracture and a molten region at the outer rim of the particle. Larger plastic deformations accompanied by lower degrees of element erosions are obtained from the corresponding FE simulations, as shown in Figure 15d. Note that due to the solid mechanics nature of the simulations in this work, predictions of a molten phase were not possible. However, the deformation-induced temperature increase shown earlier in Figure 13b is an implicit indicator of the likely state transformation of the 100 kDa PS particle from a glassy solid to a viscous liquid state, resulting in the formation of the molten phase observed in SEM images.

5. SUMMARY AND CONCLUSIONS

Results presented and discussed in previous sections demonstrate that the deposition mechanisms of glassy PS particles are complex, strongly dependent on molecular weight, and governed by the interplay between plastic deformation (and its consequent phenomena, e.g., local temperature increase, solid to liquid transformation, etc.[21,22]), and particle fracture. Although the role of the former is established as one of the primary bond formation and deposition mechanisms in the cold spray process, our findings suggest that the latter is of no less significance, at least in the cold spray of relatively brittle glassy thermoplastics. As such, an optimized solvent-free, solid-state deposition of glassy polymers by cold spray requires an in-depth understanding and analysis of the co-existence and competing effects of plastic deformation and material fracture. Highlighted by the results of the present experimental modeling study, the following remarks can be used as guidelines for such analyses:

Particles with lower molecular weights possess lower resistance to plastic deformation and fracture. However, their failure strains are more significantly affected by molecular weight. Therefore, the lower molecular weight PS particles show substantial failure and fragmentation upon impact on a stiff substrate. Upon impact, the larger failed volume of the particle acts as an effective mechanism to lower the kinetic energy, eventually causing deposition on such stiff substrates.

Particles with higher molecular weights are relatively more resistant to plastic deformation (i.e., higher yield stress and hardening coefficients) while being significantly more ductile. Regardless of the substrate stiffness, the higher molecular weight PS particles undergo larger plastic deformations, showing higher local heating effects. Large plastic deformation of the particle in a like-on-like impact was shown by both model and experiment to be insufficient for a successful deposition. The plastically deformable nature of the PS substrate that causes insufficient thermal softening and recoiling of PS particles is the factor impeding the deposition in PS-on-PS impact.

Switching the PS substrate with a rigid Si substrate was shown to promote deposition. This behavior was explained through the significant effect of an undeformed substrate, leading to the development of larger plastic deformations, higher temperature, and more prominent softening of the particle, collectively increasing the likelihood and quality of the deposition.

Although not investigated in detail in the present work, the role of material viscosity in the strength of bonds formed between the PS particle and different substrates is imperative. Induced by large plastic deformations, local temperatures can increase well above the glass transition temperature of the particle, even approaching the nominal melting temperature. Low molecular weight PS tends to possess lower viscosity in the rubbery state. Such low viscosities can potentially lead to higher success in particle−substrate adhesion.

The strong interconnections between molecular weight and the plastic yielding versus brittle fracture of the glassy polymer system examined herein offer an opportunity to optimize the material−process relations for improved polymer cold spray processing conditions.

AUTHOR INFORMATION

Corresponding Author

Behrad Koohbor − *Department of Mechanical Engineering and Advanced Materials and Manufacturing Institute, Rowan University, Glassboro, New Jersey 08028, United States;* orcid.org/0000-0002-5787-4644; Email: koohbor@rowan.edu

Authors

Jeeva Muthulingam − *Department of Mechanical Engineering, Rowan University, Glassboro, New Jersey 08028, United States;* orcid.org/0000-0002-6998-9748

Anuraag Gangineri Padmanaban − *Department of Mechanical and Industrial Engineering, University of Massachusetts, Amherst, Massachusetts 01003, United States;* orcid.org/0000-0002-0684-9799

Nand K. Singh − *Department of Mechanical Engineering and Advanced Materials and Manufacturing Institute, Rowan University, Glassboro, New Jersey 08028, United States*

Tristan W. Bacha − *Department of Chemical Engineering and Advanced Materials and Manufacturing Institute, Rowan University, Glassboro, New Jersey 08028, United States*

Joseph F. Stanzione, III − *Department of Chemical Engineering and Advanced Materials and Manufacturing Institute, Rowan University, Glassboro, New Jersey 08028, United States;* orcid.org/0000-0003-0464-835X

Francis M. Haas − *Department of Mechanical Engineering and Advanced Materials and Manufacturing Institute, Rowan University, Glassboro, New Jersey 08028, United States;* orcid.org/0000-0001-7511-0392

Ratneshwar Jha − *Department of Mechanical Engineering and Advanced Materials and Manufacturing Institute, Rowan University, Glassboro, New Jersey 08028, United States*

Jae-Hwang Lee − *Department of Mechanical and Industrial Engineering, University of Massachusetts, Amherst, Massachusetts 01003, United States;* orcid.org/0000-0002-2546-1044

https://doi.org/10.1021/acsomega.2c06617
ACS Omega 2023, 8, 3956−3970

Complete contact information is available at:
https://pubs.acs.org/10.1021/acsomega.2c06617

Notes

The authors declare no competing financial interest.

■ ACKNOWLEDGMENTS

We gratefully acknowledge the financial support of the United States Army Research Laboratory through Cooperative Agreement W911NF-19-2-0152. The views and conclusions contained in this document are those of the authors and should not be interpreted as representing the official policies, either expressed or implied, of the U.S. Army Research Laboratory or the U.S. Government. The U.S. Government is authorized to reproduce and distribute reprints for Government purposes notwithstanding any copyright notation herein.

■ REFERENCES

(1) Papyrin, A., Kosarev, V., Klinkov, S., Alkhimov, A., Fomin, V. M.*Cold spray technology*; Elsevier, 2006.
(2) Assadi, H.; Kreye, H.; Gärtner, F.; Klassen, T. Cold spraying–A materials perspective. *Acta Mater.* **2016**, *116*, 382−407.
(3) Assadi, H.; Schmidt, T.; Richter, H.; Kliemann, J.-O.; Binder, K.; Gärtner, F.; Klassen, T.; Kreye, H. On parameter selection in cold spraying. *J. Therm. Spray Technol.* **2011**, *20*, 1161−1176.
(4) Bush, T. B.; Khalkhali, Z.; Champagne, V.; Schmidt, D. P.; Rothstein, J. P. Optimization of cold spray deposition of high-density polyethylene powders. *J. Therm. Spray Technol.* **2017**, *26*, 1548−1564.
(5) Khalkhali, Z.; Xie, W.; Champagne, V. K.; Lee, J.-H.; Rothstein, J. P. A comparison of cold spray technique to single particle micro-ballistic impacts for the deposition of polymer particles on polymer substrates. *Surf. Coat. Technol.* **2018**, *351*, 99−107.
(6) Gardon, M.; Latorre, A.; Torrell, M.; Dosta, S.; Fernández, J.; Guilemany, J. M. Cold gas spray titanium coatings onto a biocompatible polymer. *Mater. Lett.* **2013**, *106*, 97−99.
(7) Chen, C.; Xie, X.; Xie, Y.; Yan, X.; Huang, C.; Deng, S.; Ren, Z.; Liao, H. Metallization of polyether ether ketone (PEEK) by copper coating via cold spray. *Surf. Coat. Technol.* **2018**, *342*, 209−219.
(8) Yang, G.; Xie, W.; Huang, M.; Champagne, V. K.; Lee, J.-H.; Klier, J.; Schiffman, J. D. Polymer particles with a low glass transition temperature containing thermoset resin enable powder coatings at room temperature. *Ind. Eng. Chem. Res.* **2018**, *58*, 908−916.
(9) Singh, N. K.; Uddin, K. Z.; Muthulingam, J.; Jha, R.; Koohbor, B. A Modeling Study of Bonding Mechanisms Between Similar and Dissimilar Materials in Cold Spraying on Polymeric Substrates. *J. Therm. Spray Technol.* **2022**, *31*, 508−524.
(10) Shah, S.; Lee, J.; Rothstein, J. P. Numerical simulations of the high-velocity impact of a single polymer particle during cold-spray deposition. *J. Therm. Spray Technol.* **2017**, *26*, 970−984.
(11) Singh, N. K.; Uddin, K. Z.; Muthulingam, J.; Jha, R.; Koohbor, B. Analyzing the Effects of Particle Diameter in Cold Spraying of Thermoplastic Polymers. *J. Therm. Spray Technol.* **2021**, *30*, 1226−1238.
(12) Nikbakht, R.; Seyedein, S. H.; Kheirandish, S.; Assadi, H.; Jodoin, B. Asymmetrical bonding in cold spraying of dissimilar materials. *Appl. Surf. Sci.* **2018**, *444*, 621−632.
(13) Xie, Y.; Yin, S.; Chen, C.; Planche, M.-P.; Liao, H.; Lupoi, R. New insights into the coating/substrate interfacial bonding mechanism in cold spray. *Scr. Mater.* **2016**, *125*, 1−4.
(14) Ko, K. H.; Choi, J. O.; Lee, H. The interfacial restructuring to amorphous: A new adhesion mechanism of cold-sprayed coatings. *Mater. Lett.* **2016**, *175*, 13−15.
(15) Assadi, H.; Gärtner, F.; Stoltenhoff, T.; Kreye, H. Bonding mechanism in cold gas spraying. *Acta Mater.* **2003**, *51*, 4379−4394.
(16) Viscusi, A.; Astarita, A.; Gatta, R.; Rubino, F. A perspective review on the bonding mechanisms in cold gas dynamic spray. *Surf. Eng.* **2019**, *35*, 743−771.
(17) Zhu, L.; Jen, T.-C.; Pan, Y.-T.; Chen, H.-S. Particle bonding mechanism in cold gas dynamic spray: a three-dimensional approach. *J. Therm. Spray Technol.* **2017**, *26*, 1859−1873.
(18) Grujicic, M.; Saylor, J. R.; Beasley, D. E.; DeRosset, W. S.; Helfritch, D. Computational analysis of the interfacial bonding between feed-powder particles and the substrate in the cold-gas dynamic-spray process. *Appl. Surf. Sci.* **2003**, *219*, 211−227.
(19) Bae, G.; Kumar, S.; Yoon, S.; Kang, K.; Na, H.; Kim, H. -J.; Lee, C. Bonding features and associated mechanisms in kinetic sprayed titanium coatings. *Acta Mater.* **2009**, *57*, 5654−5666.
(20) Ravi, K.; Ichikawa, Y.; Ogawa, K.; Deplancke, T.; Lame, O.; Cavaille, J.-Y. Mechanistic study and characterization of cold-sprayed ultra-high molecular weight polyethylene-nano-ceramic composite coating. *J. Therm. Spray Technol.* **2016**, *25*, 160−169.
(21) Shan, W.; Xiao, K.; Thomas, E. L. Influence of entanglements on ultrahigh strain rate deformation of polystyrene microprojectiles. *Macromolecules* **2022**, *55*, 9594−9600.
(22) Padmanaban, A. G.; Bacha, T. W.; Muthulingam, J.; Haas, F. M.; Stanzione, J. F., III; Koohbor, B.; Lee, J. -H. Molecular-Weight-Dependent Interplay of Brittle-to-Ductile Transition in High-Strain-Rate Cold Spray Deposition of Glassy Polymers. *ACS Omega* **2022**, *7*, 26465−26472.
(23) Rahmati, S.; Ghaei, A. The use of particle/substrate material models in simulation of cold-gas dynamic-spray process. *J. Therm. Spray Technol.* **2014**, *23*, 530−540.
(24) Wang, X.; Feng, F.; Klecka, M. A.; Mordasky, M. D.; Garofano, J. K.; El-Wardany, T.; Nardi, A.; Champagne, V. K. Characterization and modeling of the bonding process in cold spray additive manufacturing. *Addit. Manuf.* **2015**, *8*, 149−162.
(25) Oyinbo, S. T.; Jen, T.-C. Investigation of the process parameters and restitution coefficient of ductile materials during cold gas dynamic spray (CGDS) using finite element analysis. *Addit. Manuf.* **2020**, *31*, 100986.
(26) Lee, S. F.; Swallowe, G. M. Quasi-static and dynamic compressive behavior of poly(methyl methacrylate) and polystyrene at temperatures from 293 K to 363 K. *J. Mater. Sci.* **2006**, *41*, 6280−6289.
(27) Zhang, X.; Binqiang, L.; Gang, W.; Guiji, W.; Fuli, T.; Jianheng, Z.; Chengwei, S. Yield behavior of polystyrene at strain rate 106/s under quasi-isentropic compression. *Mech. Mater.* **2018**, *124*, 1−6.
(28) Rosch, T. W.; Brennan, J. K.; Izvekov, S.; Andzelm, J. W. Exploring the ability of a multiscale coarse-grained potential to describe the stress-strain response of glassy polystyrene. *Phys. Rev. E* **2013**, *87*, 042606.
(29) Hasegawa, H.; Ohta, T.; Ito, K.; Yokoyama, H. Stress-strain measurement of ultra-thin polystyrene films: Film thickness and molecular weight dependence of crazing stress. *Polymer* **2017**, *123*, 179−183.
(30) Yokouchi, M.; Uchiyama, H.; Kobayashi, Y. Effect of tensile strain rate on the mechanical properties of polystyrene and high-impact polystyrene. *J. Appl. Polym. Sci.* **1980**, *25*, 1007−1015.
(31) Wu, J. J.; Buckley, C. P. Plastic deformation of glassy polystyrene: A unified model of yield and the role of chain length. *J. Polym. Sci. B Polym. Phys.* **2004**, *42*, 2027−2040.
(32) Cook, D. G.; Rudin, A. Fracture mechanics parameters for polystyrene under high speed impact. *Polym. Eng. Sci.* **1990**, *30*, 596−602.
(33) Wool, R. P.; O'Connor, K. M. A theory of crack healing in polymers. *J. Appl. Phys.* **1981**, *52*, 5953−5963.
(34) Bacha, T. W.; Manuguerra, D. C.; Marano, R. A.; Stanzione, J. F. Hydrophilic modification of SLA 3D printed droplet generators by photochemical grafting. *RSC Adv.* **2021**, *11*, 21745−21753.
(35) Lee, J.-H.; Veysset, D.; Singer, J. P.; Retsch, M.; Saini, G.; Pezeril, T.; Nelson, K. A.; Thomas, E. L. High strain rate deformation of layered nanocomposites. *Nat. Commun.* **2012**, *3*, 1164.
(36) Lee, J.-H.; Loya, P. E.; Lou, J.; Thomas, E. L. Dynamic mechanical behavior of multilayer graphene via supersonic projectile penetration. *Science* **2014**, *346*, 1092−1096.

(37) Chen, Q.; Alizadeh, A.; Xie, W.; Wang, X.; Champagne, V.; Gouldstone, A.; Lee, J. -H.; Müftü, S. High-Strain-Rate Material Behavior and Adiabatic Material Instability in Impact of Micron-Scale Al-6061 Particles. *J. Therm. Spray Technol.* **2018**, *27*, 641−653.
(38) Yin, S.; Wang, X. F.; Li, W. Y.; Jie, H. E. Effect of substrate hardness on the deformation behavior of subsequently incident particles in cold spraying. *Appl. Surf. Sci.* **2011**, *257*, 7560−7565.
(39) Maxwell, B.; Nguyen, M. Measurement of the elastic properties of polymer melts. *Polym. Eng. Sci.* **1979**, *19*, 1140−1150.
(40) Schollenberger, C. S.; Dinbergs, K. Thermoplastic Polyurethane Elastomer Molecular Weight-Property Relations. Further Studies. *J. Elastomers Plastics* **1979**, *11*, 58−91.

https://doi.org/10.1021/acsomega.2c06617
ACS Omega 2023, 8, 3956−3970